Jiaxian Li[1], Pengcheng Zhou[1], Junping Ren[1], Yiqing Pu[1], Fanyu Zhang[1], and Chong Wang[1]

[1]College of Civil Engineering and Mechanics, Lanzhou University

March 07, 2024

Abstract

Unfrozen water content (UWC) is a key parameter affecting a variety of soil physical-mechanical properties and processes in frozen soil systems. However, traditional estimation models suffer limitations due to oversimplified assumptions or limited applicable conditions. Given that, there is a compelling need to explore alternative modeling approaches that leverage machine learning (ML) algorithms, which have shown increasing potential in engineering fields. To this end, this study evaluated and compared six widely known ML algorithms (i.e., three ensemble models: RF, LightGBM and XGBoost; and three non-ensemble models: KNN, SVR and BPNN) for modeling UWC based on collected experimental datasets. These algorithms were optimized and evaluated using a framework combining Bayesian optimization and cross-validation to ensure model stability and generalization. The results demonstrated that the ensemble tree-based methods, particularly LightGBM and XGBoost, achieved the highest predictive accuracy and superior overall performance. On the other hand, the nonensemble methods exhibited poorer generalization abilities. Interestingly, during 10-fold cross-validation, consistent underperformance was observed for a particular fold, possibly stemming from the challenges of the data distribution in that fold after random shuffling. The present study highlights the effectiveness of ensemble learning approaches, importance of proper hyperparameter tuning and validation strategies, and intrinsic modeling challenges arising from the difference between the freezing and thawing phase change behaviors. This comprehensive ML model comparison and robust training framework provide valuable guidance on selecting suitable data-driven techniques for modeling frozen soil properties for cold regions hydrogeology and engineering practices.

Unfrozen Water Content Estimation: A Comparison between Ensemble and Non-ensemble Machine Learning Models

Jiaxian Li, Pengcheng Zhou, Junping Ren*, Yiqing Pu, Fanyu Zhang, Chong Wang

College of Civil Engineering and Mechanics, Lanzhou University, Lanzhou 730000, China

*Corresponding author: Junping Ren

Email: renjp@lzu.edu.cn

Abstract:

Unfrozen water content (UWC) is a key parameter affecting a variety of soil physical-mechanical properties and processes in frozen soil systems. However, traditional estimation models suffer limitations due to oversimplified assumptions or limited applicable conditions. Given that, there is a compelling need to explore alternative modeling approaches that leverage machine learning (ML) algorithms, which have shown increasing potential in engineering fields. To this end, this study evaluated and compared six widely known ML algorithms (i.e., three ensemble models: RF, LightGBM and XGBoost; and three non-ensemble models: KNN, SVR and BPNN) for modeling UWC based on collected experimental datasets. These algorithms were optimized and evaluated using a framework combining Bayesian optimization and cross-validation to ensure model stability and generalization. The results demonstrated that the ensemble tree-based methods, particularly LightGBM and XGBoost, achieved the highest predictive accuracy and superior overall performance. On the other hand, the non-ensemble methods exhibited poorer generalization abilities. Interestingly, during 10-fold cross-validation, consistent underperformance was observed for a particular fold, possibly stemming from the challenges of the data distribution in that fold after random shuffling. The present study highlights the effectiveness of ensemble learning approaches, importance of proper hyperparameter tuning and validation strategies, and intrinsic modeling challenges arising from the difference between the freezing and thawing phase change behaviors. This comprehensive ML model comparison and robust training framework provide valuable guidance on selecting suitable data-driven techniques for modeling frozen soil properties for cold regions hydrogeology and engineering practices.

Keywords: *Unfrozen water content; Machine learning; Ensemble learning; Bayesian optimization; Model comparison*

1. Introduction

The freezing of water to form ice is one of the most common phase transformations in the natural environment (Wettlaufer, 1999). At a negative temperature, not all pore water in a soil undergoes transformation into ice; rather, a certain amount of liquid water exists because of capillarity and the surface energy of soil particles, which is termed as unfrozen water (Xu et al., 2001). The relationship between unfrozen water content (UWC) and subzero temperature is typically referred to as the soil-freezing characteristic curve (SFCC) (Ren et al., 2021). The variation of UWC during freezing–thawing process significantly influences the thermal, hydraulic and mechanical properties of frozen soils. It is also often accompanied with water migration (Zhang et al., 2018b), frost heave (Li et al., 2018; Ren et al., 2023a; Pei et al., 2024), and thaw settlement (Zhang and Michalowski, 2015; Liu et al., 2024) of the frozen soil system, which potentially leads to geological disasters as well as poses great threats to the infrastructures and environment in cold regions. Therefore, the accurate determination of UWC in frozen soils is of great scientific and practical importance in cold region hydrogeology and engineering practices.

The UWC in frozen soils depends on plenty of factors, including soil properties (e.g., mineral composition, soil pore size distribution, water content, density, composition and concentration of pore solution), and external conditions which include environmental temperature, pressure, and freezing-thawing and drying-wetting histories (Xu et al., 2001; Tian et al., 2014; Kong et al., 2020). In addition, due to the hysteresis effect between the freezing and thawing branches of SFCC, the UWC at the same subzero temperature often exhibit differences (Zhang et al., 2020; Li JX et al., 2024). The complicated effects of these factors and their intricate interactions on UWC result in difficulties associated with the convenient and precise measurement of UWC in frozen soils, under either the laboratory or in-situ

62 conditions. Therefore, many studies have shifted their focus towards developing UWC estimation

63 models, including empirical relations fitted to experimental data, semi-empirical relations based on soil-

64 water characteristic curve (SWCC), and models derived from various theories (e.g., Mckenzie et al.,

65 2007; Liu and Yu, 2013; Wang C et al., 2017; Bai and Lai, 2018; Li Z et al., 2020).

66   For example, Anderson and Tice (1972) proposed an empirical model, wherein the UWC is

67 regarded as a simple power function of subzero temperature. However, the model parameters need to

68 be determined by experiments and lack physical meanings (Kong et al., 2020; Wan et al., 2022). To

69 address these limitations, Kong et al. (2020) proposed a piecewise function consisting of a linear

70 equation and a power equation to describe SFCC. In addition, the equation proposed by Anderson and

71 Tice tends to infinity at freezing temperatures close to 0 °C, rendering it unacceptable in numerical

72 modeling of frozen soil behavior. Instead, Michalowski (1993) proposed an exponential equation taking

73 into account the residual UWC, which was adopted by Zhang and Michalowski (2015) for thermo-

74 hydro-mechanical analysis of frost heave and thaw settlement. By combining the simplified Clapeyron

75 equation with the Brooks and Corey (1964) SWCC equation, Sheshukov and Nieber (2011) obtained a

76 relationship for UWC and subzero temperature. Chai et al. (2018) considered the UWC as the sum of

77 unfrozen capillary water and unfrozen bound water, and proposed calculation equations based on the

78 freezing points of these two components. Jin et al. (2020) established a theoretical model for quantify

79 UWC based on independent variables of temperature, specific surface area and electrical double-layer

80 parameters. Wan et al. (2022) employed the premelting theory to investigate the variation in unfrozen

81 water during soil freezing, which provides a new idea to determining UWC. However, these prediction

82 models derived from experimental data and physical theories suffer from a limited application scope,

83 restricting their utility to specific soils and thus falling to meet the requirements for widespread practical

application. Addressing these issues is imperative to enhancing our understanding of the complex behavior of water-ice transition in soils during freezing and thawing, potentially paving the way for the development of more precise models for UWC prediction (Zou et al., 2023).

In order to address the aforementioned challenges and develop UWC models with broader applicability, some studies have taken advantage of machine learning (ML) techniques. Shang and Mao (2001) proposed a model based on backpropagation neural network (BPNN) to predict the empirical parameters of the SFCC of Morin Clay under different initial water content, dry density and NaCl concentration. Based on experimental data obtained by nuclear magnetic resonance, Liu et al. (2018) constructed two models using adaptive network fuzzy inference system (ANFIS) and BPNN to predict the UWC of saline soil. Wang Q et al. (2020) proposed a new model to predict the UWC of saline soil based on the combined weighting method and ANFIS. Ren Z et al. (2023) established a model based on the genetic algorithm and BPNN to predict UWC under extremely-low-temperature conditions. Ren et al. (2023b) proposed a BPNN modeling framework for predicting the UWC in various types of soils, based on the collected large amount of experimental data. However, neural networks (NNs) sometimes yield "random" UWC predictions that violate physical mechanisms. To address this issue, Li JX et al. (2024) adopted a constrained monotonic neural network to ensure the predicted UWC decreases as the temperature decreases. However, the algorithms employed in these studies are mainly limited to NNs. In addition, other ML methods, which have been successfully used in the prediction of landslide susceptibility as well as soil properties (e.g., Chen et al., 2017; Baghbani et al., 2022), show potential use in UWC estimation (Nartowska and Sihag, 2024). Therefore, it is imperative to evaluate and compare the performance of various ML algorithms and determine the most suitable algorithmic models for predicting UWC.

106   In our previous study (Ren et al., 2023b), the hysteresis of SFCC was ignored for simplicity and

107   the freezing and thawing UWC data were combined to train a BPNN model for estimating UWC. A key

108   limitation of this approach stems from the inconsistency between the target values at the same input

109   condition, since the UWC at the same subzero temperature exhibit differences during the freezing and

110   thawing processes, thereby introducing a source of prediction error in the developed model. Therefore,

111   in this study, the experimental UWC data of freezing and thawing branches are separately collected

112   from literature to alleviate this concern. Based on these two datasets, six mainstream ML algorithms

113   (i.e., Random Forest (RF), eXtreme Gradient Boosting (XGBoost), Light Gradient Boosting Machine

114   (LightGBM), K-Nearest Neighbors (KNN), Support Vector Regression (SVR), and BPNN) were

115   employed to estimate UWC in frozen soils. The first three algorithms are ensemble learning methods

116   and the rest three are non-ensemble. To ensure model stability and generalization, a framework combing

117   Bayesian optimization and 10-fold cross-validation was used to optimize algorithm hyperparameters

118   and evaluate model performance. The six models were comprehensively compared in terms of their

119   predictive abilities and other quantitative metrics. The advantages and limitations of each approach are

120   critically discussed regarding their suitability for modeling complex soil behavior using freezing and

121   thawing datasets. The results of the present study can guide the selection of suitable data-driven

122   techniques for modeling frozen soil properties. The overall modeling framework is summarized in Fig.

123   1.

124

125   **2. Dataset preparation**

126   In the present study, soil physical properties and the UWC data were obtained from the literature.

127   The raw data were extracted from the original plots depicting the UWC-Subzero temperature relations

128   (i.e., SFCC) using the GetData Graph Digitizer. More details regarding the collected data can be found

129   in Ren et al. (2023b). The freezing or thawing process was generally measured in the selected studies,

130   while several studies measured both the freezing and thawing SFCC branches (e.g., Kozlowski and

131   Nartowska, 2013; Ren and Vanapalli, 2019; Teng et al., 2020). However, due to hysteresis between

132   freezing and thawing processes, the same soil sample often exhibits different UWC values at the same

133   subzero temperature. This causes difficulties in ML development since identical inputs corresponding

134   to different outputs in the training data, hindering effective model training and compromising the

135   robustness of the trained model. To avoid this obstacle, the dataset collected from studies that measured

136   both branches was divided into separate freezing and thawing subsets. For studies employing multiple

137   measurement methods, only the data based on NMR measurements were retained, as it is a relatively

138   stable and accurate method to measure UWC without damaging the soil samples (Ren et al., 2020; He

139   et al., 2023). Additionally, for studies measuring UWC under multiple freeze-thaw cycles, only the

140   UWC measurements on either the freezing or thawing branch of the first cycle were included in the

141   database. As a result, two separate datasets were obtained: the freezing branch dataset (FBD) and the

142   thawing branch dataset (TBD). The FBD and TBD comprise 790 and 1410 UWC data points,

143   respectively. All subsequent analysis and discussions in this study will be based on these two separate

144   datasets.

145

146   **2.1 Data statistical description**

147   Similar to the study by Ren et al. (2023b), the following four factors influencing UWC were

148   considered: specific surface area (SSA), dry density (ρ_d), initial volumetric water content (θ_{ini}), and

149   subzero temperature (*Temp*). The statistical features of the two datasets (i.e., FBD and TBD) are

150 described next. Table 1 summarizes key statistical descriptors of the four input variables and the output

151 (i.e., UWC) for both the freezing and thawing data subsets. The standard deviation, SD, representing

152 the arithmetic square root of the variance, serves as a measure of the extent to which observations

153 deviate from their mean. Skewness, Sk, presents distribution characteristics, with positive Sk suggesting

154 a bias towards larger-than-average data points, while negative Sk signifies a prevalence of observations

155 below the mean. Additionally, Kurtosis (Ku) provides insights into the tail distribution, where high Ku

156 indicates heavy tails and potential outliers, while low kurtosis points to lighter tails with fewer extreme

157 values compared to a normal distribution (Li and Vanapalli, 2022; Li JX et al., 2024). These statistical

158 values are calculated based on Eqs. (1) to (3):

159
$$SD = \sqrt{\frac{\sum_{i=1}^{n}\left(X_i - \overline{X}\right)^2}{n}} \tag{1}$$

160
$$S_k = \frac{n}{(n-1)(n-2)}\sum_{i=1}^{n}\left(\frac{X_i - \overline{X}}{SD}\right)^3 \tag{2}$$

161
$$K_u = \frac{n(n+1)}{(n-1)(n-2)(n-3)}\sum_{i=1}^{n}\left(\frac{X_i - \overline{X}}{SD}\right)^4 - \frac{3(n-1)^2}{(n-2)(n-3)} \tag{3}$$

162 where n is the total number of a variable, X_i and $\overline{X}$ are the value and mean of the variable, respectively.

163 Figure 2 presents the histograms as well as kernel density plots of the four variables and the

164 prediction target (i.e., θ_u). The FBD exhibits high variability and non-normal distributions for several

165 key variables. The input feature SSA and the output θ_u exhibit positive skewed distributions, which

166 indicates substantial right-tailed distributions, as evidenced by their Sk values (see Table 1) and kernel

167 density curves. The distribution of θ_{ini} is close to a normal distribution. Meanwhile, ρ_d and *Temp* show

168 negative skewed distributions with their Sk values below -1, indicating left-tailed shapes. The Ku values

169 of SSA, ρ_d, *Temp*, and θ_u exceeding 3 further demonstrate heavy tails and large values. In comparison,

170 the TBD displays different data distributions. The SSA and θ_u retain strong positive skewness and heavy

171 tails seen in Fig. 2(a) & (d), and the distribution of SSA becomes steeper compared to a normal

172 distribution. The θ_{ini} has a slightly positive skewed distribution while ρ_d shows minor negative skewness.

173 Unlike FBD, the kernel density curves for these two variables in TBD exhibit two peaks (see Fig. 2(b)

174 & (c)), indicating that the distributions of these two variables are more complex or multimodal

175 compared to those in FBD. Although the two datasets share some statistical similarities in their means

176 and SDs, the freezing data overall displays more pronounced non-normal distributions and heavy-tailed

177 characteristics. These statistical differences highlight the unique characteristics inherent between the

178 collected freezing and thawing data.

179

180 **2.2 Feature importance**

181   The frozen soil is a complicated four-phase system and the amount of unfrozen water in a frozen

182 soil is a regression function of multiple variables. Therefore, it is necessary to identify how much each

183 factor affects the UWC and which factor influences the UWC most. Since UWC depends on the intricate

184 interplay of multiple influencing factors, resulting in a complex non-linear relationship among them,

185 and the Spearman correlation coefficient (SCC) serves as a nonparametric or distribution-free statistical

186 measure to describe the rank of variables (Xiao et al., 2016; Li KQ et al., 2022), herein, Spearman

187 correlation analysis was adopted to analyze the correlation degree between the four input variables and

188 the output. The SCC can be calculated as:

189
$$SCC = 1 - \frac{6\sum d_i^2}{n(n^2 - 1)} \tag{4}$$

190 where d_i is the difference between each pair of the ranked variables and n is the total sample size of

191 observations.

192 Figure 3 shows the correlation relationship among the input variables and the output for the two

193 datasets. Temperature exerts the predominant control on UWC in both the freezing and thawing

194 processes, with SCC values of 0.59 and 0.61, respectively. Dry density (ρ_d) has the least effect on UWC

195 during both processes and was negatively correlated, with SCC values of -0.07 and -0.22, respectively.

196 However, well-defined correlations were not observed between any input variable and the UWC. This

197 is because the interactions between the influencing factors are intricate and not yet fully understood.

198 Therefore, the UWC prediction does not typically depend on any single factor (Li JX et al., 2024).

199 Notably, for the freezing process, θ_{ini} has a greater effect than the SSA, whereas the converse is observed

200 for the thawing process. In the freezing process, the initial liquid water content determines the total

201 amount of water available for phase transition to ice. However, during thawing, the vast majority of the

202 initial water has transformed into the ice phase, therefore its direct influence on UWC diminishes.

203 Instead, the SSA, which quantifies the surface area contact between ice and soil particles, becomes

204 more impactful. A higher SSA provides more surface for conducting heat transfer and water flow during

205 thawing. This shift in the relative importance of influential factors again indicates the differences

206 between the freezing and thawing processes.

207

208 **3. Models overview and development**

209 **3.1 Six machine learning algorithms**

210 A wide variety of ML algorithms have been developed for multivariate regression modeling. For

211 this study, six representative ML algorithms were employed to model and predict UWC: RF, XGBoost,

212 LightGBM, KNN, SVR and BPNN, with the first three being ensemble models and the rest three non-

213 ensemble. The selection of these six ML algorithms is motivated by their diverse strengths and

214   capabilities. The RF, XGBoost, and LightGBM were specifically chosen as ensemble models can

215   achieve stronger predictive performance by combining multiple weak learners. Complementing the

216   ensemble models, we include KNN, SVR, and BPNN, each renowned in ML prediction tasks for their

217   distinct approaches, ensuring a thorough exploration of diverse modeling strategies for UWC prediction.

218   The subsequent sections provide succinct overviews of the underlying principles, as well as general

219   advantages and limitations of each ML algorithms.

220

221   3.1.1 Random forest (RF)

222   The RF method was developed by Breiman (2001) as an expansion of the classification and

223   regression trees technique to provide better performance of prediction results. The RF is an extended

224   algorithm that combines multiple decision trees (DTs) based on the bagging idea of ensemble learning,

225   which enhances basic models' diversity by considering a random set of features at splitting nodes (Li

226   KQ et al., 2022). As schematically illustrated in Fig. 4, the learners (i.e., DTs) are trained separately on

227   the training dataset, and their individual outputs are combined to form the final learning result, with

228   each sample holding equal weight. For regression problems, the final output of RF is the average of the

229   outputs generated by all DTs. The benefits of employing RFs are that the ensembles of trees are used

230   without pruning. In addition, this method is relatively robust to overfitting (Zhang et al., 2020).

231

232   3.1.2 Extreme gradient boosting (XGBoost)

233   The XGBoost is an improved optimization algorithm based on Gradient Boosting Decision Tree

234   (GBDT), as proposed by Chen and Guestrin (2016). In the field of machine learning, it is well

235   recognized that the XGBoost is currently one of the fastest and best open sources boosted tree

236 algorithms. The basic element of XGBoost is the single decision tree and its mechanism is to keep

237 adding and training new trees to fit residuals of last iteration (Dong et al., 2020), as shown in Fig. 5.

238 Compared with GBDT, the XGBoost performs second-order Taylor expansion of the loss function to

239 improve calculation accuracy, and adds a regularization term (i.e., Eq. (6)) to the objective function to

240 prevent overfitting and control the complexity of the model (Yang et al., 2023). Equation 5 evaluates

241 the model "goodness" relative to the original function (Fan et al., 2021).

$$Obj = \sum_{i=1}^{n} l(y_i, \bar{y}_i) + \sum_{k=1}^{K} \Omega(f_k) \tag{5}$$

243 where, *Obj* represents the objective function, *l* is the loss function, *K* represents the total number of

244 decision trees, f_k represents the complexity of the kth tree, and *Ω* is the regularization term, which is

245 expressed as:

$$\Omega(f) = \gamma T + \frac{1}{2}\lambda \|\omega\|^2 \tag{6}$$

247 where, *ω* is the score vector, *λ* is the regularization parameter, and *γ* is the mini loss.

248

249 3.1.3 Light gradient boosting machine (LightGBM)

250 Although XGBoost is regarded as a state-of-the-art evaluator with ultra-high performance in both

251 classification and regression tasks, its efficiency and scalability are not satisfactory in the presence of

252 high feature dimensions and large data sizes (Wu, 2020; Wang et al., 2021). In contrast, LightGBM,

253 released by Microsoft in late 2017 (Ke et al., 2017), emerges as a novel gradient boosting technique

254 designed to address the limitations of traditional boosting algorithms, including high memory usage,

255 computational complexity and time consumption (Sun et al., 2022).

256 Differing from XGBoost, the LightGBM leverages Histogram-based techniques to discretize

257 continuous eigenvalues into multiple integers (also called bins). It performs the gradient accumulation

258   and counting according to the bin where the eigenvalues are located, and then iterates over all the

259   eigenvalues to find the optimal splitting point. This not only improves efficiency but also reduces

260   memory occupation. The discrete split points also have a regularization effect, which could effectively

261   reduce the over-fitting phenomenon for small datasets (Qiu et al., 2023). In addition, based on the

262   Histogram algorithm, the LightGBM implements a leaf-wise algorithm with depth limitation to split

263   the leaf nodes instead of the level-wise technique for growing decision trees. Specifically, in contrast

264   to the level-wise algorithm, which traverses the data once and then splits each leaf of the level, the leaf-

265   wise algorithm first determines which leaf within the level will provide the biggest splitting gain and

266   subsequently performs the split, as shown in Fig. 6. This strategy reduces the complexity of the model,

267   maintains a high-efficiency level, and simultaneously enhances the resistance to overfitting

268   (Hajihosseinlou et al., 2023). Furthermore, the LightGBM uses the gradient-based one-side sampling

269   algorithm and the mutually exclusive feature bundling algorithm to solve the problems of excessive

270   number of samples and features respectively, which further improves the computational efficiency of

271   the model. The LightGBM is also frequently used in data mining competition, such as Kaggle, where

272   it has proven to be a winning solution (Ustuner and Balik, 2019; Cai et al., 2022). For more in-depth

273   explanations of LightGBM, readers can refer to Ke et al. (2017).

274

275   **3.1.4 K-nearest neighbors (KNN)**

276   The KNN algorithm is one of the simplest ML algorithms in terms of both underlying principles

277   and, often, computational demand. As a nonparametric classifier introduced by Cover and Hart (1967),

278   the KNN is based on labeling the unknown instance using known instances. At the stage of classification

279   for a given new sample, the KNN algorithm searches through all training samples and then computes

280   the distances between the target sample and each training data point to determine the nearest neighbors

281   and produce the classification output (Yamac et al., 2020). Typically, the Euclidean distance algorithm

282   is used to calculate the distances between instances (Araya and Ghezzehei, 2019).

283   For a simple classification task shown in Fig. 7, when $k = 3$, there are two triangles and one circle

284   in the nearest neighborhood of the unknown class. Consequently, the unknown class is determined to

285   be Class B. While $k = 5$, the category becomes Class A. When applied for regression problems, KNN

286   predicts the value of a new instance by averaging the values of its "k" nearest (i.e., most similar)

287   neighbors in the training data. The KNN is considered as a nonparametric algorithm since it does not

288   assume an underlying data distribution. However, the KNN does not perform any generalization on the

289   training data and retains all data points, which may result in overfitting. Additionally, the need for

290   distance computation of k-nearest neighbors makes the algorithm computationally intensive with large

291   datasets, limiting its scalability (Ray, 2019; Zhao et al., 2022). Moreover, the KNN algorithm is highly

292   sensitive to redundant and irrelevant features and therefore feature selection must be done carefully

293   (Yamac et al., 2020).

294

295   **3.1.5 Support vector regression (SVR)**

296   Support vector machine (SVM), as a type of generalized linear classifiers proposed by Cortes and

297   Vapnik (1995), is derived from the structural risk minimization hypothesis to minimize both empirical

298   risk and the confidence interval of the learning machine for improved generalization capability. The

299   SVM is developed based on statistical learning theory, the basic idea of which is to map the original

300   datasets from the input space to a high-dimensional or even infinite-dimensional feature space, in order

301   to define a separable hyperplane that maximizes the margin between classes, such that the classification

302 problem becomes simpler in the feature space (Raghavendra and Deka, 2014; Hosseinzadeh et al., 2021).

303 The function that transforms data from input space to feature space is called the kernel function. The

304 SVM model requires the data to be located in this hyperplane as much as possible to minimize the total

305 deviation of all the data from the hyperplane. Additionally, the SVM method uses a small number of

306 support vectors instead of the entire sample space, which makes it easier to calculate the final decision

307 function with improved robustness and efficiency. Compared with complex NNs, the SVM has

308 demonstrated better performance and requires fewer hyperparameters to be tuned while avoiding local

309 minima (Khlosi et al., 2016; Wang F et al., 2020).

310 Although the SVM was developed to solve classification tasks, it has been extended to regression

311 scenarios (Smola and Schölkopf, 1998), which is known as the support vector regression (SVR). For

312 regression problems, the SVR introduces an ε-insensitive loss function to determine a hyperplane,

313 which allows for some deviation between the predicted and target values without affecting loss

314 calculation. In other words, the loss is calculated only when the absolute value of the difference between

315 predictions and targets is greater than ε (Lu and Wang, 2023). As shown in Fig. 8, values centered on

316 the function and within the error range on either side of it are considered correctly predicted, while only

317 values outside the dash line are incorporated into loss computation and model updating process.

318

319 **3.1.6 Backpropagation neural network (BPNN)**

320 The BPNN is a well-known learning method for multi-layer feedforward neural network trained

321 by an error backpropagation algorithm (Li J et al., 2012). The BPNN was first proposed by Paul Werbos

322 in 1974 and later popularized by Rumelhart et al. (1986). The BPNN can not only simulate various

323 nonlinear relationships between variables, but also has self-adaptability and self-learning capabilities.

324   As shown in Fig. 9, a complete BPNN consists of input layer, hidden layers and output layer. The

325   number of neurons in the hidden layers largely affects the performance of BPNNs. Specifically, each

326   neuron in the hidden layer receives the weighted combination of input values from the preceding layer

327   and calculates an output depending on the activation function, which is then propagated as the input to

328   neurons in the next hidden layer. This process can be mathematically represented as:

329
$$y_j = f\left(\sum_{i=1}^{n} w_i x_i + b\right) \tag{7}$$

330   where x_i is the value of neurons in the previous layer, w_i represents weights, b represents bias, f is

331   activation function, and y_j is the output of the current neuron.

332   The training of BPNN includes two key processes: forward propagation of the input signals and

333   backpropagation of error. In the forward propagation, information flows from the input layer to the

334   output layer (Kurt and Kayfeci, 2009). And during backpropagation, the error between the predictions

335   from the forward pass and target values is calculated and then propagated back to the input layer to

336   update weights (Feng et al., 2015). The activation function also plays an important role in the training

337   and performance of the model, as it determines the output of the neurons based on their input. It provides

338   the necessary nonlinearity for the model to represent complex functions. Commonly used activation

339   functions include the rectified linear unit (ReLU) function (Eq. (8)), as used in this study, along with

340   the sigmoid and hyperbolic tangent (tanh) function.

341
$$\text{ReLU}(x) = max(0, x) \tag{8}$$

342   Despite its powerful learning ability and popularity, the BPNN has limitations such as being prone

343   to falling into local optimum (Liu et al., 2013), which causes the training of BPNN being more sensitive

344   to the initial network weights (Tongle et al., 2016).

345

3.2 Bayesian optimization and cross-validation

The above six ML algorithms were employed to construct models based on the freezing branch dataset (FBD) and the thawing branch dataset (TBD). To facilitate subsequent model evaluation, 90 and 160 data points were selected randomly from FBD and TBD respectively, forming the freezing test dataset (FBD_test) and the thawing test dataset (TBD_test). The remaining data were used for models training and validation. Specifically, the rest 700 data points from the original FBD were used as the freezing training-validation dataset (FBD_train-val), while the rest 1250 data points from the original TBD were used as the thawing training-validation dataset (TBD_train-val).

Before models training, all model inputs and outputs should generally be standardized. The purpose of this is to avoid excessive network prediction error due to the large order of magnitude difference between different features (Raju et al., 2020), as well as arguably to make the algorithms converge faster. Therefore, we utilized StandardScaler from the scikit-learn preprocessing library to standardize both the FBD and TBD. The StandardScaler standardizes features by removing the mean and scaling to unit variance. The underlying principle of standardization can be described by the following equation:

$$X_{norm} = \frac{X - \overline{X}}{SD} \tag{9}$$

As noted by Zhang et al. (2020), standardization or normalization is unnecessary for RFs because they are insensitive to the range of inputs. Since DT-based models focus on the distribution of variables and conditional probabilities between them, rather than the raw values, normalization is not required. In fact, for RF, LightGBM, XGBoost and other DT-based models, data normalization has little effect on output results, which has been observed in several studies (Coulston et al., 2012). Therefore, in this study, data standardization was not performed prior to establishing the three DT-based ensemble models.

368   The predictive performance of ML models depends on the appropriate combinations of

369   hyperparameters, such as the number of regression trees and the number of random variables of nodes

370   (i.e., *Max depth*) in RFs. Hyperparameter optimization is fundamentally a problem of optimizing a

371   specific mapping function over graph-structured configuration space (Zhang et al., 2021). While the

372   significance of hyperparameters is evident, manually exploring the optimum hyperparameter

373   combinations requires experienced insight and can be tedious (Kim et al., 2022). In response to this

374   challenge, Bayesian optimization (BO) emerges as an efficient solution to hyperparameter tuning

375   problem by searching through hyperparameter candidates. The core technique of BO lies in utilizing

376   the prior probability of the objective function and observation points to update the posterior probability

377   distribution and then find the next minimal value point with a more posterior probability distribution

378   and get the optimal hyperparameter through iterations (Zhang et al., 2023). Since new candidates are

379   selected based on the results from previous hyperparameters, the best combination of hyperparameters

380   can be configured in less time and fewer evaluations than grid search or random search (Li and Kanoulas,

381   2018). Therefore, in this study, the BO was employed to fine-tune the hyperparameters of each model

382   to maximize performance. For the automated search for optimal hyperparameter configurations during

383   model training, we utilized the Hyperopt Python library, leveraging its sequential model-based

384   optimization (SMBO) technique powered by the Tree of Parzen Estimators (TPE) algorithm. This

385   enabled efficient tuning tailored to each model's unique configuration needs.

386   In addition, we strategically incorporated 10-fold cross-validation (CV) within the BO framework

387   to assess the generalization capabilities of models under each identified hyperparameter combination

388   obtained during the BO process. More specifically, the 10-fold CV process categorizes both FBD_train-

389   val and TBD_train-val into ten equal-sized datasets randomly. In the case of FBD_train-val, a dataset

390   with 630 data points was utilized for training the six ML models, while the remaining 70 data points

391   were for validation. Similarly, for TBD_train-val, a dataset with 1125 and 125 data points was used for

392   training and validation, respectively. This procedure was repeated 10 times with one of the 10 folds

393   served as the validation dataset each time, and 10 validation performance scores were generated for

394   every hyperparameter candidate. The hyperparameter configuration that achieved the highest average

395   score was then selected as the optimal setting for the model. It is undeniable that incorporating 10-fold

396   CV into the framework of BO increases computational cost and runtime for finding the optimal

397   hyperparameters of models. Hence, for the candidate hyperparameters of BPNN, we opted not to set a

398   continuous range but specifying common discrete values. Additionally, the number of Bayesian

399   iterations affects the running times of the whole model (Stephens and Donnelly, 2003). The iteration

400   number was consistently set to 100 in this study to save computational cost.

401   Three performance indicators were adopted to evaluate the performance of the above six models:

402   coefficient of determination (R^2), root mean square error (RMSE) and mean absolute percentage error

403   (MAPE). The R^2 indicator measures the level of fitness between the target and model prediction values.

404   The RMSE is more sensitive to large errors between the target and prediction, due to the quantification

405   by using squared difference. In contrast, the MAPE demonstrates low sensitivity to outliers, which

406   makes it a suitable indicator for data with anticipated outliers (Huang et al., 2023). The three model

407   indicators can be calculated as follows:

408
$$R^2 = 1 - \frac{\sum_{i=1}^{n}(y_i - \hat{y}_i)^2}{\sum_{i=1}^{n}(y_i - \overline{y}_i)^2} \tag{10}$$

409
$$RMSE = \sqrt{\frac{1}{n}\sum_{i=1}^{n}(y_i - \hat{y}_i)^2} \tag{11}$$

$$MAPE = \frac{100\%}{n} \sum_{i=1}^{n} \frac{|y_i - \hat{y}_i|}{|\hat{y}_i|} \tag{12}$$

where n is the number of samples, y_i is the target value, $\hat{y}_i$ is the prediction value, and $\bar{y}$ is the average

value of y.

To assess the stability of the models, we calculated the average R^2, RMSE and MAPE of the 10

folds. The 10-fold average R^2 in validation was used as the score metric for BO. Once the optimal

hyperparameter combinations were identified, models with the optimal hyperparameters were saved (to

avoid model weights being updated again) and used to predict UWC based on FBD_test and TBD_test.

As mentioned previously, these two datasets were separated from the dataset before model training and

validation, hence representing new and unseen data for the established models. Since 10-fold CV was

incorporated in the BO process, there were 10 test results. The final predicted results were calculated

by weighted averaging the test results from each fold, where the weights were the R^2 values on the

validation set. This weighted approach was implemented to mitigate potential disparities in performance

among different folds, ensuring a balanced representation of the overall model performance. The

calculation formula is expressed as:

$$P_{final} = \frac{\sum_{i=1}^{10} P_i \bullet R_i^2}{\sum_{i=1}^{10} R_i^2} \tag{13}$$

where, P_{final} is the final predicted result, P_i is the test result from Fold i, R_i^2 is the R^2 value on the

validation set for Fold i, and i ranges from 1 to 10.

For the purpose of benchmarking the six ML models against the test data, the Taylor diagram was

used as an effective tool. It can provide a concise visualization of statistical relationship between the

models' predictions and targets, through the correlation coefficient, the centered pattern root-mean-

square error (CRMSE) and standard deviation (Taylor, 2001; Hu et al., 2020).

431

4. Results and analysis

Optimizing hyperparameters is crucial for achieving optimal performance in ML algorithms. However, due to the high dimensionality of the hyperparameter space, exhaustively searching all combinations in the hyperparameter space is computationally expensive and time-consuming. Therefore, only the most influential hyperparameters on model performance were considered and selected for optimization in this study. Table 2 summarizes the key hyperparameters of each ML algorithm and their corresponding optimized values based on FBD_train-val and TBD_train-val. The following analysis utilized these models configured with the optimal hyperparameter combination.

The average R^2 and RMSE values obtained through the 10-fold CV for each model on FBD and TBD during training and validation are summarized in Tables 3 and 4, respectively. The ensemble tree-based models (i.e., RF, LightGBM, XGBoost) demonstrated excellent performance in predicting UWC on both datasets, as evidenced by high R^2 values exceeding 0.97 and low RMSE values below 0.02 during training, indicating strong goodness-of-fit. Among the ensemble models, the LightGBM achieved the highest average training R^2 values of 0.9956 on FBD and 0.9870 on TBD, with RMSE values of 0.0075 and 0.0112, respectively. The XGBoost and RF closely followed with outstanding performance. In contrast, non-ensemble models (KNN, SVR, and BPNN) did not perform as well as the ensemble methods. Their training R^2 scores on FBD ranged from 0.91 to 0.94, with higher RMSE values between 0.025 and 0.035. Specifically, the SVR scored high training R^2 value of 0.9387 and achieved low training RMSE value of 0.0283, outperforming the other two non-ensemble models.

As shown in Fig. 10, the three ensemble methods also performed better than non-ensemble models in validation processes, with R^2 values ranging from 0.85 to 0.90 and low RMSE values. In FBD_val,

453   the LightGBM led with an R^2 value of 0.8601 and an RMSE value of 0.0388. Conversely, for TBD_val,

454   the XGBoost obtained the highest R^2 of 0.8970 with the lowest RMSE. However, non-ensemble models

455   exhibited a decline in performance, with R^2 values dropping to 0.80-0.83 and RMSE values rising to

456   above 0.04, indicating an increase in variance and minor overfitting compared to ensemble models.

457   Among the non-ensemble models, the KNN exhibited the poorest performance on TBD_val (R^2 =

458   0.7663 and RMSE = 0.0464), despite achieving a training R^2 value of 0.9006. This suggests that KNN

459   may be less effective at capturing the complex relationships between the input variables and UWC, and

460   is more prone to overfitting compared to SVR and BPNN. Summing up the comparison of model

461   performance on training and validation sets, the generalization abilities of ensemble tree-based methods

462   on new data are better than their non-ensemble counterparts.

463   In order to get more insights on the models' performance, their R^2 results of the 10-fold CV on the

464   two validation datasets (i.e., FBD_val and TBD_val) are depicted in Fig. 11. Interestingly, the validation

465   results show that all models exhibited poorer performance consistently on the 3rd fold compared to

466   others when evaluated on FBD_val (see Fig. 11 (a)). The drop is most pronounced for the KNN, with

467   an R^2 of 0.506 on the 3rd fold compared to its highest R^2 value of 0.9111 – indicating a gap over 0.4.

468   The other models exhibited smaller yet evident decrease on the 3rd fold. In contrast, the worst validation

469   fold generally shifts to the 4th fold when models are evaluated on TBD_val. Notably, the degree of

470   underperformance on the 4th fold improved for all models compared to FBD_val, although the KNN

471   still demonstrated the largest discrepancy on this fold. For the BPNN and XGBoost, the worst validation

472   result on TBD_val occurred in the 10th fold rather than the 4th fold, as shown in Fig. 11(b).

473   It is worth mentioning that, although the BPNN obtained the lowest training R^2 of 0.9132 and

474   0.8736 on the two datasets, its R^2 values on the validation sets (i.e., 0.8273 and 0.8161) are the highest

475 among the three non-ensemble models. This implies that BPNN has the lowest degree of overfitting

476 and may have better captured the underlying data patterns. However, it may benefit from additional

477 training data for enhanced performance. In addition, the higher R^2 values of BPNN on the two validation

478 sets compared with that reported in Ren et al. (2023b) (i.e., 0.76) indicates that separately training

479 models based on the freezing and thawing branch datasets could potentially improve model

480 performance.

481   In Fig. 12, a visual representation compares the target values versus the predictions by the six

482 models on the two test datasets. It is evident that the non-ensemble learning models, particularly KNN,

483 exhibit a larger number of data points deviating from the 1:1 line compared to the ensemble learners,

484 indicating their slightly inferior predictive performance. Figure 13 gives a more straightforward

485 comparison of the six models in terms of their R^2, RMSE and MAPE on the test datasets. Overall, most

486 models achieved satisfactory predictive performance with R^2 values above 0.8 on FBD_test, except for

487 the SVR. Specifically, the LightGBM notably achieved the highest R^2 with the lowest RMSE,

488 outperforming the other five models in terms of accuracy. It also attained the lowest MAPE value of

489 0.36, indicating a superior ability in minimizing error rates. Followed closely, the XGBoost secured

490 with an R^2 of 0.861, an RMSE of 0.031 and an MAPE of 0.384. However, models' performance on

491 TBD_test exhibited varying results, with the XGBoost achieving the top R^2 and lowest MAPE, clearly

492 demonstrating strongest predictive accuracy on this dataset. The LightGBM also maintained excellent

493 performance with R^2, RMSE and MAPE values of 0.888, 0.031 and 0.306, respectively. Among the

494 other four models, the KNN performed the worst with the lowest R^2, the highest RMSE and the second-

495 highest MAPE. This positions it as the model with the poorest performance and the lowest accuracy on

496 TBD_test. The performance of the SVR and BPNN on this test dataset is similar, as evidenced by their

RMSE values, both of which are 0.041. The significant discrepancy in the model performance between the two test datasets can be attributed to the distinct nature of the datasets' distributions and inherent patterns. Referring to Figs. 12 and 13, the LightGBM performs best in this comparative analysis on both test datasets, outperforming the other five models employed in this study.

Figure 14 is the Taylor diagrams that provide useful diagnostic comparisons between the six ML models' predictions and targets. The reference variable of the Taylor diagrams is the target UWC in test datasets (the REF point on the horizontal axis). It can be seen that the LightGBM obtained the highest correlation coefficient while the RF had the smallest standard deviation on FBD_test. The performance gap between the six models is not large on this test dataset. On TBD_test, however, the models' performance is more discrete, and the KNN achieved the lowest correlation coefficient, far away from the other models as well as the REF point.

5. Discussion

In this study, the collected UWC data were partitioned into separate freezing and thawing datasets. The statistical analysis revealed distinct distributions between the two datasets, suggesting significant differences in their underlying features. This split is justified physically that different mechanisms govern the change of UWC in soil freezing and thawing processes. The former is influenced chiefly by temperature, while the latter becomes more affected by soil particle properties such as SSA. For example, the correlation between SSA and UWC jumps from 0.2 on the FBD to 0.46 on the TBD (see Fig. 3). In addition, although the complicated mechanisms responsible to the hysteresis have not been thoroughly revealed, the difference between the freezing and thawing SFCC branches does manifest, especially in the high subzero temperature range (Tian et al., 2014; Zhou et al., 2018; Ren and Vanapalli,

519   2020). This means that for the same subzero temperature, the corresponding UWC on the freezing

520   branch is higher than that on the thawing branch. Therefore, the amalgamation of freezing-thawing

521   UWC dataset for training ML models introduces potential risks of ambiguous input-output mappings.

522   That is, the same input corresponds different targets in the training dataset, which may compromise the

523   stability and robustness of models during training. Additionally, this uncertainty could lead to notable

524   fluctuations in the models' prediction for a given input, or, the trained model may struggle to generalize

525   to new, unseen data, as it is hard for it to produce correct output for the same input scenarios. This

526   limitation can adversely affect the model's performance when applied to real-world situations. Hence,

527   the reasonable spilt of the freezing and thawing data enables the ML models to better capture the

528   inherent laws of changes in UWC during the freezing and thawing processes, and improve the accuracy

529   of prediction.

530   The 10-fold CV was integrated within BO to determine the optimal hyperparameter configuration

531   for each model. This framework enables maximizing the potential of each optimized model for fair

532   comparison rather than relying solely on the performance based on a single random split. In other words,

533   the cross-validation is effective in avoiding the impacts of the randomness of dataset division and

534   ensuring the robustness of the trained model. And to a certain extent, it can also help mitigate overfitting

535   and underfitting. However, the application of the 10-fold CV in BO does impose additional

536   computational expense which may become prohibitive for inherently slower models like NNs.

537   Therefore, when optimizing the hyperparameters of BPNN in this study, we did not set a continuous

538   parameter range like the other five models. Instead, we opted for specific, predetermined values, such

539   as restricting the number of hidden layers to discrete options like 1, 2, and 3, depending on the question

540   investigated. This strategy was made to strike a good balance between the efficient exploration of the

541 hyperparameter space and the reduction of generalization error for subsequent comparison between

542 models.

543   The noteworthy underperformance on the third fold during the 10-fold CV of models built on FBD

544 warrants further investigation. One potential explanation is that in this fold, the validation data

545 distribution pattern is rather distinctive, encompassing a greater number of particular samples, such as

546 more outliers or noisy data, compared to the training data. That is, models may be less capable of

547 generalizing to the validation data in Fold 3 due to insufficient similar samples in the training data of

548 this fold. In contrast, during the CV of models based on TBD, most models exhibited poorest

549 performance on the fourth fold. This shift partially highlights the difference in data distribution between

550 the freezing and thawing datasets. The above phenomenon could also be attributed to some problems

551 in parameters and hyperparameters tuning for the models. It is plausible that models require different

552 parameter settings for optimal performance based on underlying distribution and pattern of the training

553 data in Fold 3, which emphasizes the importance of carefully selecting and tuning parameters during

554 ML tasks. Furthermore, this observation reflects the potential for models to experience notable

555 performance drops under certain dataset spilt, which demonstrates the necessity of using the 10-fold

556 CV in this study to assess model robustness and generalizability.

557   Moreover, it is also possible that subtle overfitting effects may have occurred which negatively

558 impact models' performance during the validation process. Taking the performance of models based

559 on FBD_train-val as an example, the high R^2 and low RMSE values during the training process on the

560 Fold 3 imply adequate model fitting. As shown in Table 5, however, the performance of all models on

561 unseen data in the validation set has significantly decreased, indicating a potential occurrence of

562 overfitting. This overfitting tendency is not exclusive to the validation set, but extending to the test sets

563   (i.e., FBD_test and TBD_test). Comparing Table 3 and Figure 13 reveals a notable decline in predictive

564   performance of models on the two test sets compared to the training sets, accompanied by a significant

565   increase in errors, where the R^2 difference is approximately 10%. Despite employing the weighted

566   approach to obtain the final test results, this potential overfitting phenomenon still occurs in two test

567   sets, which would be mitigated through the augmentation of dataset size by collecting additional data

568   or the introduction of regularization techniques to the models.

569   Among the six ML models, the KNN exhibited its poorest performance on Fold 3 of the FBD_val

570   and Fold 4 of the TBD_val, displaying notable disparities compared to other folds. This discrepancy

571   suggests that the performance of KNN may be significantly influenced by the local structure of the data.

572   As a nonparametric algorithm, KNN relies solely on a few nearest training samples (i.e., its

573   "neighbors"), making it susceptible to the influence of outliers when the value of k is small (Abu Alfeilat

574   et al., 2019). If a particular fold contains data with substantial variations or non-uniform distribution in

575   specific regions, KNN may exhibit poor performance in that fold. Furthermore, the performance of

576   KNN may be highly influenced by the selection of hyperparameters, such as the number of neighbors

577   (i.e., k). Different folds may necessitate varying numbers of neighbors to adapt to changes in the local

578   data structure. Consequently, considerable variations in performance may be observed in the 10-fold

579   CV. Therefore, when employing the KNN algorithm, it is suggested that special attention should be

580   paid to the handling of outliers and noise.

581   The LightGBM and XGBoost, as highly optimized gradient boosting algorithms, demonstrated

582   superior predictive power on both FBD and TBD. These algorithms iteratively fit new models to

583   emphasize previously mispredicted instances, thereby incrementally optimizing the ensemble as a

584   whole. Although the overall performance of the RF is not as good as the above two boosting models,

585 its performance is superior to that of the non-ensemble models. This is expected as ensemble learning

586 algorithms like random forests and boosting methods (e.g., LightGBM and XGBoost) combine multiple

587 weaker models to create an overall stronger model, reducing variance (Skurichina and Duin, 2002;

588 Ferreira and Figueiredo, 2012). Specifically, taking the RF as an example, it averages predictions from

589 an ensemble of decorrelated decision trees grown on random subsets of the data and features, which

590 helps reduce variance relative to a single decision tree model. In contrast, the non-ensemble methods

591 such as KNN, SVR, and BPNN did not exhibit such predictive advantages. The predictions of KNN

592 rely on the average of the k nearest neighbors. However, in the study, Bayesian optimization results

593 indicate that the optimal values for the number of neighbors (i.e., k value) in KNN are 2 and 3 on

594 FBD_train and TBD_train, respectively (refer to Table 2). Such relatively small k values may make

595 models more susceptible to noisy data and outliers, so that KNN yielded unreasonable predictions. The

596 SVR and BPNN, while possessing universal approximation properties, are prone to overfitting given

597 challenges associated with hyperparameter optimization and lack of ensemble effect. However, as

598 mentioned in Section 4, the BPNN did display competitive capability in UWC prediction among the

599 three non-ensemble algorithms. This can be attributed to its robust and strong power to model complex

600 nonlinear relationships, stemming from its multilayer structure and the application of the

601 backpropagation algorithm during training.

602   In summary, the ensemble approaches provided the most effective and robust solutions for the

603 prediction task in this study because of their ability to synergistically combine multiple simple basic

604 learners, especially the gradient boosting methods. The three non-ensemble models manifested

605 relatively poorer performance, even though the 10-fold CV strategy ensured their robustness and

606 stability. Further hyperparameter tuning and diverse ensemble techniques could help the non-ensemble

models boost predictive accuracy and achieve better generalization, on the assignment of estimating UWC in frozen soils. Future work may explore how to effectively connect the freezing and thawing sub-models into a unified framework to capture the complexity of soil behaviors.

6. Summary

In this study, the UWC data collected from the literature was partitioned into separate freezing and thawing datasets. Based on the two datasets, six machine learning models were developed and evaluated for estimating UWC in frozen soils, including RF, LightGBM, XGBoost, KNN, SVR and BPNN. To ensure the robustness and generalizability of models, the integrated 10-fold CV and BO framework was employed to assess the stability of models and identify optimal hyperparameters across different data splits.

The results demonstrated that the three ensemble models (RF, LightGBM and XGBoost) achieved superior accuracy and satisfactory generalization abilities, owing to their synergistic integration of multiple basic learners. The LightGBM and XGBoost displayed the top prediction power on both the freezing and thawing test datasets. Despite slightly lower scores, the RF also exhibited reliable performance. On the other hand, the non-ensemble algorithms including KNN, SVR and BPNN performed relatively poorer in predictive accuracy compared to ensemble models, as evidenced by their lower R^2 and larger RMSE during both training and validation. Among the non-ensembles, the BPNN showcased relatively robust modeling proficiency, which attributes to its nonlinear approximation strengths. Overall, the non-ensemble methods lagged behind their ensemble counterparts.

Findings highlight the superiority and effectiveness of ensemble learning approaches, especially gradient boosting trees, for the UWC estimation task in the study. The present results provide useful

guidance on selecting and applying advanced machine learning techniques for modeling frozen soil

properties and behaviors during different processes. It underscores the importance of proper validation

strategies and accounting for distinct freezing/thawing phase change behaviors when developing data-

driven models for cold regions hydrogeology and engineering practices.

Competing Interests

The authors declare there are no competing interests.

Data Availability Statement

The data that support the findings of this study are available upon reasonable request.

References

Abu Alfeilat, H. A., Hassanat, A. B., Lasassmeh, O., Tarawneh, A. S., Alhasanat, M. B., Eyal Salman,
H. S., & Prasath, V. S. (2019). Effects of distance measure choice on k-nearest neighbor classifier
performance: a review. Big data, 7(4), 221-248.

Anderson, D. M., & Tice, A. R. (1972). Predicting unfrozen water contents in frozen soils from surface

652   area measurements. Highway Research Record, 393(2), 12-18.

653 Araya, S. N., & Ghezzehei, T. A. (2019). Using machine learning for prediction of saturated hydraulic

654   conductivity and its sensitivity to soil structural perturbations. Water Resources Research, 55(7),

655   5715-5737.

656 Baghbani, A., Choudhury, T., Costa, S., & Reiner, J. (2022). Application of artificial intelligence in

657   geotechnical engineering: A state-of-the-art review. Earth-Science Reviews, 228, 103991.

658 Bai, R., Lai, Y., Zhang, M., & Yu, F. (2018). Theory and application of a novel soil freezing

659   characteristic curve. Applied Thermal Engineering, 129, 1106-1114.

660 Breiman, L. (2001). Random forests. Machine Learning, 45, 5-32.

661 Brooks, R. H., & Corey, A. T. (1966). Properties of porous media affecting fluid flow. Journal of The

662   Irrigation and Drainage Division, 92(2), 61-88.

663 Cai, W., Wei, R., Xu, L., & Ding, X. (2022). A method for modelling greenhouse temperature using

664   gradient boost decision tree. Information Processing in Agriculture, 9(3), 343-354.

665 Chai, M., Zhang, J., Zhang, H., Mu, Y., Sun, G., & Yin, Z. (2018). A method for calculating unfrozen

666   water content of silty clay with consideration of freezing point. Applied Clay Science, 161, 474-

667   481.

668 Chen, T., & Guestrin, C. (2016, August). Xgboost: A scalable tree boosting system. In Proceedings of

669   the 22nd acm sigkdd international conference on knowledge discovery and data mining (pp. 785-

670   794).

671 Chen, W., Xie, X., Wang, J., Pradhan, B., Hong, H., Bui, D. T., ... & Ma, J. (2017). A comparative

672   study of logistic model tree, random forest, and classification and regression tree models for spatial

673   prediction of landslide susceptibility. Catena, 151, 147-160.

674 Cortes, C., & Vapnik, V. (1995). Support-vector networks. Machine Learning, 20, 273-297.

675 Coulston, J. W., Moisen, G. G., Wilson, B. T., Finco, M. V., Cohen, W. B., & Brewer, C. K. (2012).

676   Modeling percent tree canopy cover: a pilot study. Photogrammetric Engineering and Remote

677   Sensing, 78(7), 715-727.

678 Cover, T., & Hart, P. (1967). Nearest neighbor pattern classification. IEEE Transactions on Information

679   Theory, 13(1), 21-27.

680 Dong, W., Huang, Y., Lehane, B., & Ma, G. (2020). XGBoost algorithm-based prediction of concrete

681   electrical resistivity for structural health monitoring. Automation in Construction, 114, 103155.

Fan, J., Zheng, J., Wu, L., & Zhang, F. (2021). Estimation of daily maize transpiration using support vector machines, extreme gradient boosting, artificial and deep neural networks models. Agricultural Water Management, 245, 106547.

Feng, Q., Zhang, J., Zhang, X., & Wen, S. (2015). Proximate analysis based prediction of gross calorific value of coals: A comparison of support vector machine, alternating conditional expectation and artificial neural network. Fuel Processing Technology, 129, 120-129.

Ferreira, A. J., & Figueiredo, M. A. (2012). Boosting algorithms: A review of methods, theory, and applications. Ensemble Machine Learning: Methods and applications, 35-85.

Hajihosseinlou, M., Maghsoudi, A., & Ghezelbash, R. (2023). A novel scheme for mapping of MVT-type Pb–Zn prospectivity: LightGBM, a highly efficient gradient boosting decision tree machine learning algorithm. Natural Resources Research, 1-22.

Hayashi, M. (2013). The cold vadose zone: Hydrological and ecological significance of frozen-soil processes. Vadose Zone Journal, 12(4).

He, Y., Xu, Y., Lv, Y., Nie, L., Kong, F., Yang, S., ... & Li, T. (2023). Characterization of unfrozen water in highly organic turfy soil during freeze–thaw by nuclear magnetic resonance. Engineering Geology, 312, 106937.

Hosseinzadeh, A., Moeinaddini, A., & Ghasemzadeh, A. (2021). Investigating factors affecting severity of large truck-involved crashes: Comparison of the SVM and random parameter logit model. Journal of Safety Research, 77, 151-160.

Hu, G., Zhao, L., Zhu, X., Wu, X., Wu, T., Li, R., ... & Hao, J. (2020). Review of algorithms and parameterizations to determine unfrozen water content in frozen soil. Geoderma, 368, 114277.

Huang, Y., Wang, Y., Wang, P., & Lai, Y. (2023). An XGBOOST predictive model of void ratio in sandy soils with shear-wave velocity as major input. Transportation Geotechnics, 42, 101100.

Jin, X., Yang, W., Gao, X., Zhao, J. Q., Li, Z., & Jiang, J. (2020). Modeling the unfrozen water content of frozen soil based on the absorption effects of clay surfaces. Water Resources Research, 56(12), e2020WR027482.

Ke, G., Meng, Q., Finley, T., Wang, T., Chen, W., Ma, W., ... & Liu, T. Y. (2017). Lightgbm: A highly efficient gradient boosting decision tree. Advances in Neural Information Processing Systems, 30.

Khlosi, M., Alhamdoosh, M., Douaik, A., Gabriels, D., & Cornelis, W. M. (2016). Enhanced pedotransfer functions with support vector machines to predict water retention of calcareous soil.

European Journal of Soil Science, 67(3), 276-284.

Kim, D., Kwon, K., Pham, K., Oh, J. Y., & Choi, H. (2022). Surface settlement prediction for urban tunneling using machine learning algorithms with Bayesian optimization. Automation in Construction, 140, 104331.

Kong, L., Wang, Y., Sun, W., & Qi, J. (2020). Influence of plasticity on unfrozen water content of frozen soils as determined by nuclear magnetic resonance. Cold Regions Science and Technology, 172, 102993.

Kozlowski, T., & Nartowska, E. (2013). Unfrozen water content in representative bentonites of different origin subjected to cyclic freezing and thawing. Vadose Zone Journal, 12(1), vzj2012-0057.

Kurt, H., & Kayfeci, M. (2009). Prediction of thermal conductivity of ethylene glycol–water solutions by using artificial neural networks. Applied Energy, 86(10), 2244-2248.

Li, D., & Kanoulas, E. (2018, February). Bayesian optimization for optimizing retrieval systems. In Proceedings of the Eleventh ACM International Conference on Web Search and Data Mining (pp. 360-368).

Li, J., Cheng, J. H., Shi, J. Y., & Huang, F. (2012). Brief introduction of back propagation (BP) neural network algorithm and its improvement. In Advances in Computer Science and Information Engineering: Volume 2 (pp. 553-558). Springer Berlin Heidelberg.

Li, J., Ren, J., Fan, X., Zhou, P., Pu, Y., & Zhang, F. (2024). Estimation of unfrozen water content in frozen soils based on data interpolation and constrained monotonic neural network. Cold Regions Science and Technology, 218, 104094.

Li, K. Q., Liu, Y., & Kang, Q. (2022). Estimating the thermal conductivity of soils using six machine learning algorithms. International Communications in Heat and Mass Transfer, 136, 106139.

Li, S., Zhang, M., Pei, W., & Lai, Y. (2018). Experimental and numerical simulations on heat-water-mechanics interaction mechanism in a freezing soil. Applied Thermal Engineering, 132, 209-220.

Li, Y., & Vanapalli, S. K. (2022). Prediction of Soil–Water Characteristic Curves of Fine-grained Soils Aided by Artificial Intelligent Models. Indian Geotechnical Journal, 52(5), 1116-1128.

Li, Z., Chen, J., & Sugimoto, M. (2020). Pulsed NMR measurements of unfrozen water content in partially frozen soil. Journal of Cold Regions Engineering, 34(3), 04020013.

Liu, M., Wang, M., Wang, J., & Li, D. (2013). Comparison of random forest, support vector machine

and back propagation neural network for electronic tongue data classification: Application to the recognition of orange beverage and Chinese vinegar. Sensors and Actuators B: Chemical, 177, 970-980.

Liu, Q., Cai, G., Zhou, C., Yang, R., & Li, J. (2024). Thermo-hydro-mechanical coupled model of unsaturated frozen soil considering frost heave and thaw settlement. Cold Regions Science and Technology, 217, 104026.

Liu, Y., Wang, Q., Zhang, X., Song, S., Niu, C., & Shangguan, Y. (2018). Using ANFIS and BPNN methods to predict the unfrozen water content of saline soil in Western Jilin, China. Symmetry, 11(1), 16.

Liu, Z., & Yu, X. (2013). Physically based equation for phase composition curve of frozen soils. Transportation Research Record, 2349(1), 93-99.

Lu, Y., & Wang, G. (2023). A load forecasting model based on support vector regression with whale optimization algorithm. Multimedia Tools and Applications, 82(7), 9939-9959.

Michalowski, R. L. (1993). A constitutive model of saturated soils for frost heave simulations. Cold Regions Science and Technology, 22(1), 47-63.

McKenzie, J. M., Voss, C. I., & Siegel, D. I. (2007). Groundwater flow with energy transport and water–ice phase change: numerical simulations, benchmarks, and application to freezing in peat bogs. Advances in Water Resources, 30(4), 966-983.

Nartowska, E., & Sihag, P. (2024). Soft Computing Techniques for Predicting Unfrozen Water Content in Copper Contaminated Bentonites: A Comparative Study of Gaussian Process Regression, Support Vector Machine, and Random Forest Models. DOI: 10.2139/ssrn.4706976

Pei, Q. Y., Zou, W. L., Han, Z., Wang, X. Q., & Xia, X. L. (2024). Compression behaviors of a freeze–thaw impacted clay under saturated and unsaturated conditions. Acta Geotechnica, 1-18.

Qiu, Y., Wang, J., & Li, Z. (2023). Personalized HRTF prediction based on LightGBM using anthropometric data. China Communications.

Raghavendra, S., & Deka, P. C. (2014). Support vector machine applications in the field of hydrology: a review. Applied Soft Computing, 19, 372-386.

Raju, V. G., Lakshmi, K. P., Jain, V. M., Kalidindi, A., & Padma, V. (2020, August). Study the influence of normalization/transformation process on the accuracy of supervised classification. In 2020 Third International Conference on Smart Systems and Inventive Technology (ICSSIT) (pp.

729-735). IEEE.

Ray, S. (2019, February). A quick review of machine learning algorithms. In 2019 International conference on machine learning, big data, cloud and parallel computing (COMITCon) (pp. 35-39). IEEE.

Ren, J., Fan, X., Yu, X., Vanapalli, S., & Zhang, S. (2023b). Use of an artificial neural network model for estimation of unfrozen water content in frozen soils. Canadian Geotechnical Journal, 60(8), 1234-1248.

Ren, J., Vanapalli, S. K., & Han, Z. (2017). Soil freezing process and different expressions for the soil-freezing characteristic curve. Sciences in Cold and Arid Regions, 9(3), 221-228.

Ren, J., Zhang, S., Ishikawa, T., Li, S., & Wang, C. (2023a). The frost heave characteristics of a coarse-grained volcanic soil quantified by particle image velocimetry. Geoderma, 430, 116352.

Ren, J., Zhang, S., Wang, C., Ishikawa, T., & Vanapalli, S. K. (2021). The Measurement of Unfrozen Water Content and SFCC of a Coarse-Grained Volcanic Soil. Journal of Testing and Evaluation, 51(1).

Ren, Z., Liu, J., Jiang, H., & Wang, E. (2023). Experimental study and simulation for unfrozen water and compressive strength of frozen soil based on artificial freezing technology. Cold Regions Science and Technology, 205, 103711.

Rumelhart, D. E., Hinton, G. E., & Williams, R. J. (1986). Learning representations by back-propagating errors. Nature, 323(6088), 533-536.

Shang, S., & Mao, X. (2001). Prediction Model of Soil Freezing Temperature and Unfrozen Water Content Based on Back-Propagation Neural Network. Journal of Glaciology and Geocryology, 23(4): 414-418. (in Chinese)

Sheshukov, A. Y., & Nieber, J. L. (2011). One-dimensional freezing of nonheaving unsaturated soils: Model formulation and similarity solution. Water Resources Research, 47(11).

Skurichina, M., & Duin, R. P. (2002). Bagging, boosting and the random subspace method for linear classifiers. Pattern Analysis & Applications, 5, 121-135.

Smola, A. J., & Schölkopf, B. (1998). Learning with kernels (Vol. 4). Berlin, Germany: GMD-Forschungszentrum Informationstechnik.

Stephens, M., & Donnelly, P. (2003). A comparison of bayesian methods for haplotype reconstruction from population genotype data. The American Journal of Human Genetics, 73(5), 1162-1169.

Sun, Y., Zhang, F., Lin, H., & Xu, S. (2022). A Forest Fire Susceptibility Modeling Approach Based on Light Gradient Boosting Machine Algorithm. Remote Sensing, 14(17), 4362.

Taylor, K. E. (2001). Summarizing multiple aspects of model performance in a single diagram. Journal of Geophysical Research: Atmospheres, 106(D7), 7183-7192.

Teng, J., Kou, J., Yan, X., Zhang, S., & Sheng, D. (2020). Parameterization of soil freezing characteristic curve for unsaturated soils. Cold Regions Science and Technology, 170, 102928.

Tian, H., Wei, C., Wei, H., & Zhou, J. (2014). Freezing and thawing characteristics of frozen soils: Bound water content and hysteresis phenomenon. Cold Regions Science and Technology, 103, 74-81.

Tongle, X., Yingbo, W., & Kang, C. (2016). Tailings saturation line prediction based on genetic algorithm and BP neural network. Journal of Intelligent & Fuzzy Systems, 30(4), 1947-1955.

Ustuner, M., & Balik Sanli, F. (2019). Polarimetric target decompositions and light gradient boosting machine for crop classification: A comparative evaluation. ISPRS International Journal of Geo-Information, 8(2), 97.

Wan, X., Pei, W., Lu, J., Zhang, X., Yan, Z., & Pirhadi, N. (2022). Prediction of the unfrozen water content in soils based on premelting theory. Journal of Hydrology, 608, 127505.

Wang, C., Lai, Y., & Zhang, M. (2017). Estimating soil freezing characteristic curve based on pore size distribution. Applied Thermal Engineering, 124, 1049-1060.

Wang, F., Shi, Z., Biswas, A., Yang, S., & Ding, J. (2020). Multi-algorithm comparison for predicting soil salinity. Geoderma, 365, 114211.

Wang, L., Wu, J., Zhang, W., Wang, L., & Cui, W. (2021). Efficient seismic stability analysis of embankment slopes subjected to water level changes using gradient boosting algorithms. Frontiers in Earth Science, 9, 807317.

Wang, Q., Liu, Y., Zhang, X., Fu, H., Lin, S., Song, S., & Niu, C. (2020). Study on an AHP-entropy-ANFIS model for the prediction of the unfrozen water content of sodium-bicarbonate-type salinization frozen soil. Mathematics, 8(8), 1209.

Wettlaufer, J. S. (1999). Ice surfaces: macroscopic effects of microscopic structure. Philosophical Transactions of the Royal Society of London. Series A: Mathematical, Physical and Engineering Sciences, 357(1763), 3403-3425.

Wu, C. Z. (2020). Soil undrained shear strength Prediction Based on XGBoost and LightGBM Model.

Chongqing University. (in Chinese)

Xiao, C., Ye, J., Esteves, R. M., & Rong, C. (2016). Using Spearman's correlation coefficients for exploratory data analysis on big dataset. Concurrency and Computation: Practice and Experience, 28(14), 3866-3878.

Yamac, S. S., Şeker, C., & Negiş, H. (2020). Evaluation of machine learning methods to predict soil moisture constants with different combinations of soil input data for calcareous soils in a semiarid area. Agricultural Water Management, 234, 106121.

Yang, Z., He, Q., Miao, S., Wei, F., & Yu, M. (2023). Surface Soil Moisture Retrieval of China Using Multi-Source Data and Ensemble Learning. Remote Sensing, 15(11), 2786.

Zhang, M., Shi, W., & Xu, Z. (2020). Systematic comparison of five machine-learning models in classification and interpolation of soil particle size fractions using different transformed data. Hydrology and Earth System Sciences, 24(5), 2505-2526.

Zhang, W., Wu, C., Zhong, H., Li, Y., & Wang, L. (2021). Prediction of undrained shear strength using extreme gradient boosting and random forest based on Bayesian optimization. Geoscience Frontiers, 12(1), 469-477.

Zhang, X., Dai, C., Li, W., & Chen, Y. (2023). Prediction of compressive strength of recycled aggregate concrete using machine learning and Bayesian optimization methods. Frontiers in Earth Science, 11, 1112105.

Zhang, X., Zhang, M., Pei, W., & Lu, J. (2018b). Experimental study of the hydro-thermal characteristics and frost heave behavior of a saturated silt within a closed freezing system. Applied Thermal Engineering, 129, 1447-1454.

Zhang, Y., & Michalowski, R. L. (2015). Thermal-hydro-mechanical analysis of frost heave and thaw settlement. Journal of Geotechnical and Geoenvironmental Engineering, 141(7), 04015027.

Zhao, T., Liu, S., Xu, J., He, H., Wang, D., Horton, R., & Liu, G. (2022). Comparative analysis of seven machine learning algorithms and five empirical models to estimate soil thermal conductivity. Agricultural and Forest Meteorology, 323, 109080.

Zhou, Z., Ma, W., Zhang, S., Mu, Y., & Li, G. (2018). Effect of freeze-thaw cycles in mechanical behaviors of frozen loess. Cold Regions Science and Technology, 146, 9-18.

Zou, Y., Jiang, H., Wang, E., Liu, X., & Du, S. (2023). Variation and prediction of unfrozen water content in different soils at extremely low temperature conditions. Journal of Hydrology, 624,

862   129900.

863

864

Table 1. Statistical description of the two datasets

Dataset	Variable	Unit	Mean	SD	Sk	Ku
FBD	SSA	m^2/g	90.35	111.433	3.421	13.872
	θ_{ini}	m^3/m^3	0.35	0.143	0.721	1.148
	ρ_d	g/cm^3	1.54	0.304	-2.317	6.265
	$Temp$	°C	-7.78	6.519	-1.583	6.437
	θ_u	m^3/m^3	0.13	0.112	1.723	4.510
TBD	SSA	m^2/g	63.12	103.229	4.585	23.767
	θ_{ini}	m^3/m^3	0.38	0.170	0.172	-0.386
	ρ_d	g/cm^3	1.38	0.336	-0.840	0.465
	$Temp$	°C	-4.93	5.199	-1.511	1.948
	θ_u	m^3/m^3	0.11	0.098	1.665	3.341

865

Table 2. Key hyperparameters for the six ML models

Model	Key hyperparameters	Optimal values	
		Freezing	Thawing
RF	n_estimators	664	789
	max_depth	12	20
	min_samples_split	2	2
	min_samples_leaf	1	1
	max_features	1	1
LightGBM	n_estimators	768	513
	max_depth	7	7
	num_leaves	70	30
	min_child_samples	2	13
	subsample	0.66	0.73
	reg_alpha	0.02	0.02
	reg_lambda	10.17	1.14
XGBoost	n_estimators	200	726
	max_depth	7	7
	learning_rate	0.52	0.14
	subsample	0.84	0.26
	reg_alpha	0.06	0.02
	reg_lambda	27.19	17.78
KNN	algorithm	2	2
	n_neighbors	2	3
SVR	kernel function	RBF	RBF
	c	6.9	7.2
	epsilon	0.007	0.049
	gamma	6.03	7.00
BPNN	n_layer	1	1
	n_hid	64	32
	lr	0.05	0.02
	batch_size	128	128
	activation function	ReLu	ReLu
	epochs	100	100

Table 3. Models' performance on FBD

Process Models	Training		Validation	
	R^2	RMSE	R^2	RMSE
RF	0.9743	0.0183	0.8551	0.0413
LightGBM	**0.9956**	**0.0075**	**0.8601**	**0.0388**
XGBoost	0.9928	0.0097	0.8526	0.0406
KNN	0.9352	0.0291	0.8091	0.0460
SVR	0.9387	0.0283	0.8209	0.0459
BPNN	0.9132	0.0336	0.8273	0.0451

869
870
871
872
873
874

Table 4. Models' performance on TBD

Process Models	Training		Validation	
	R^2	RMSE	R^2	RMSE
RF	0.9833	0.0127	0.8766	0.0338
LightGBM	**0.9870**	**0.0112**	0.8806	0.0331
XGBoost	0.9869	0.0113	**0.8970**	**0.0311**
KNN	0.9006	0.0311	0.7663	0.0464
SVR	0.9276	0.0266	0.8140	0.0415
BPNN	0.8736	0.0351	0.8161	0.0415

875
876
877
878
879
880
881

Table 5. Models' performance on Fold 3 based on FBD

Process Models	Training		Validation	
	R^2	RMSE	R^2	RMSE
RF	0.9212	0.0330	0.6501	0.0458
LightGBM	0.9964	0.0070	0.5570	0.0515
XGBoost	0.9937	0.0093	0.6442	0.0462
KNN	0.9400	0.0288	0.5060	0.0544
SVR	0.9428	0.0282	0.7058	0.0420
BPNN	0.9212	0.0330	0.6501	0.0458

883
884 **Fig. 1 Framework for unfrozen water content estimation**
885

886
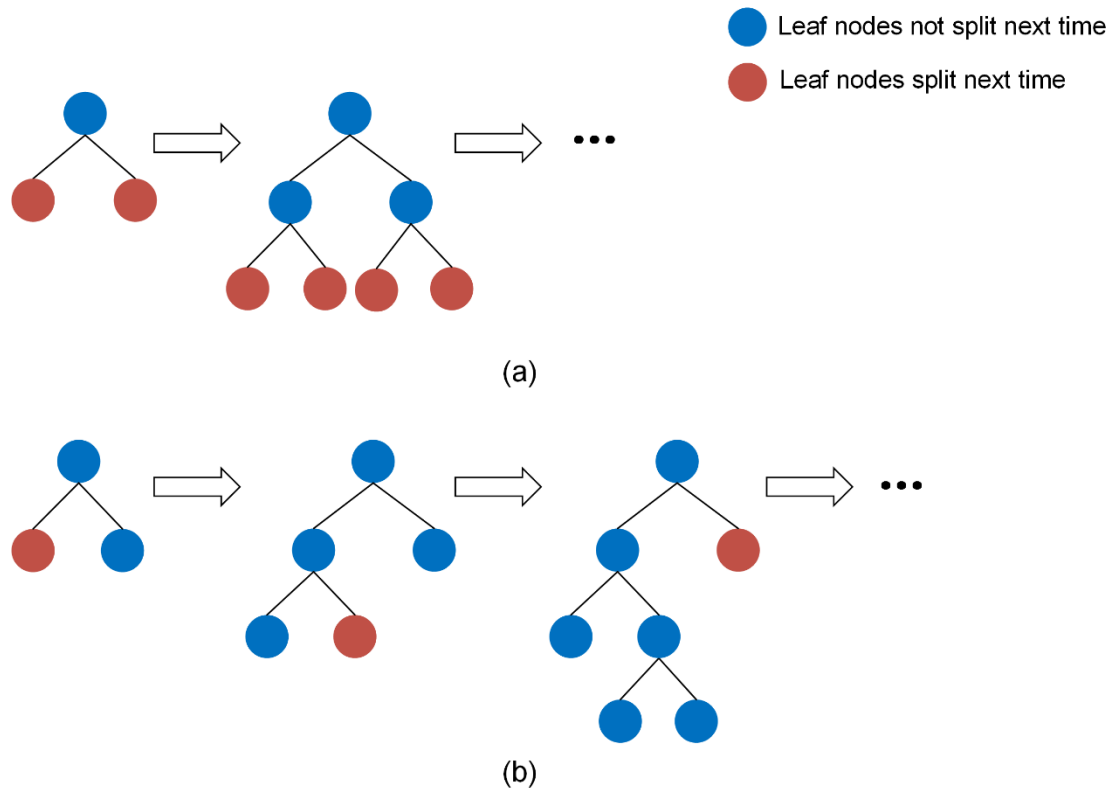887 **Fig. 2 Histogram plots of the input variables and output**
888

889

890
891 **Fig. 3 Spearman correlation coefficient heat map among variables on (a) FBD and (b) TBD**
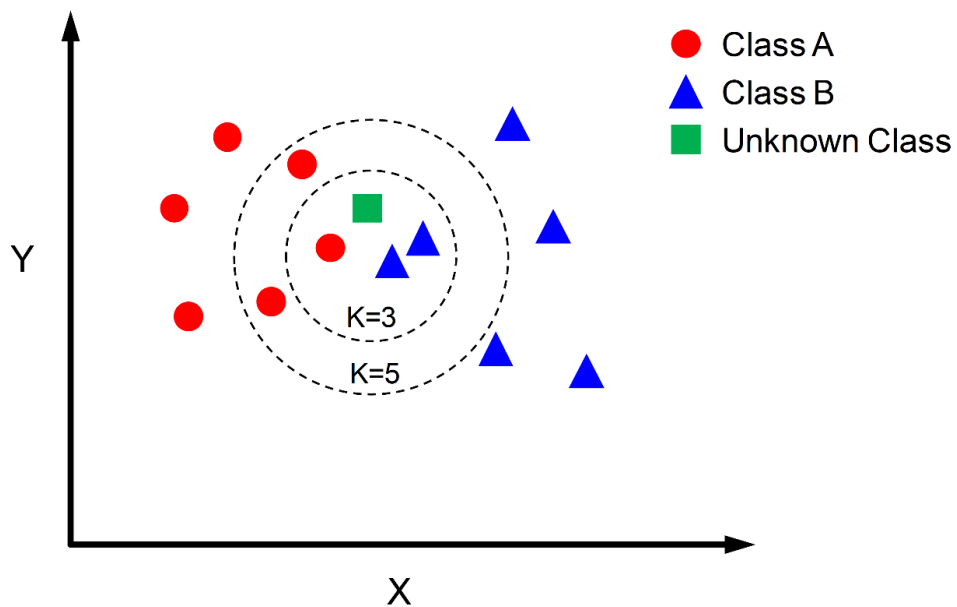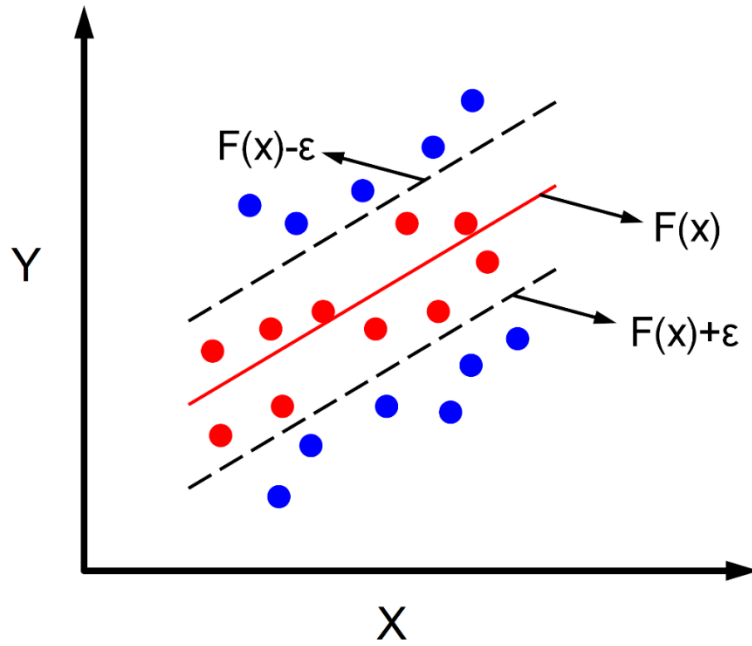892

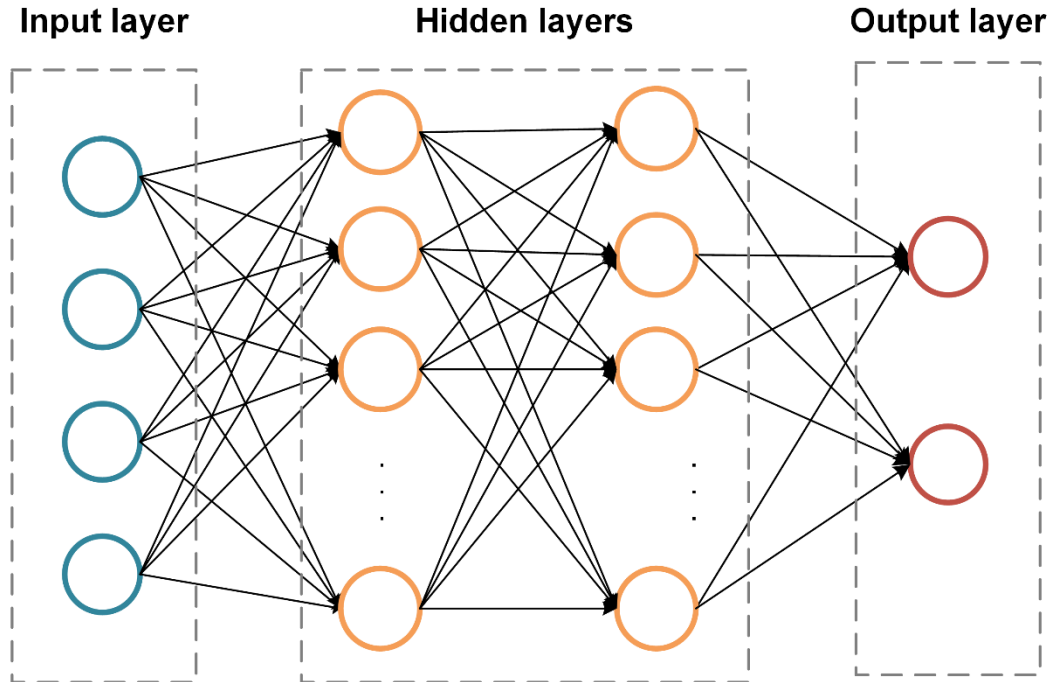Fig. 4 The structure of random forest

Fig. 5 The structure of XGBoost

(a)

(b)

899

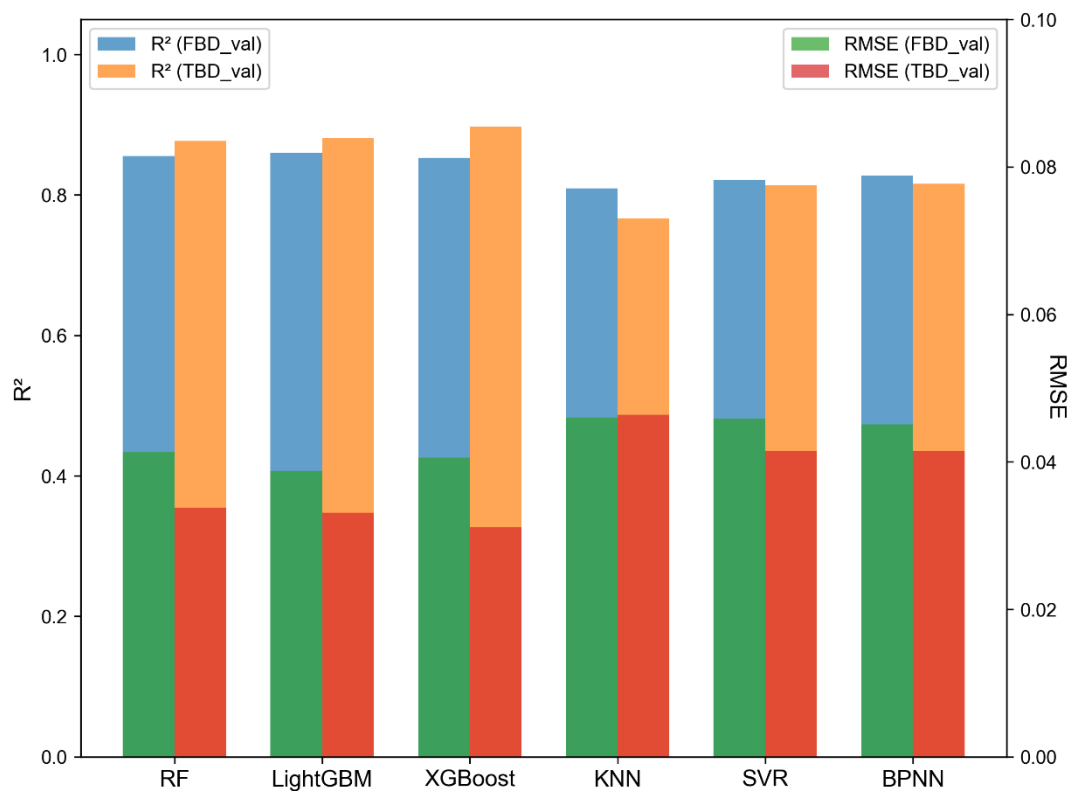900 **Fig. 6 Schematic diagram of the (a) level-wise and (b) leaf-wise algorithm**

901
902
903

904
905 **Fig. 7 Schematic diagram of KNN classification**
906

907
908 **Fig. 8 Schematic diagram of SVR hyperplane data distribution**
909
910
911
912

913
914 **Fig. 9 The structure of BPNN with input layer, hidden layers and output layer**
915

916
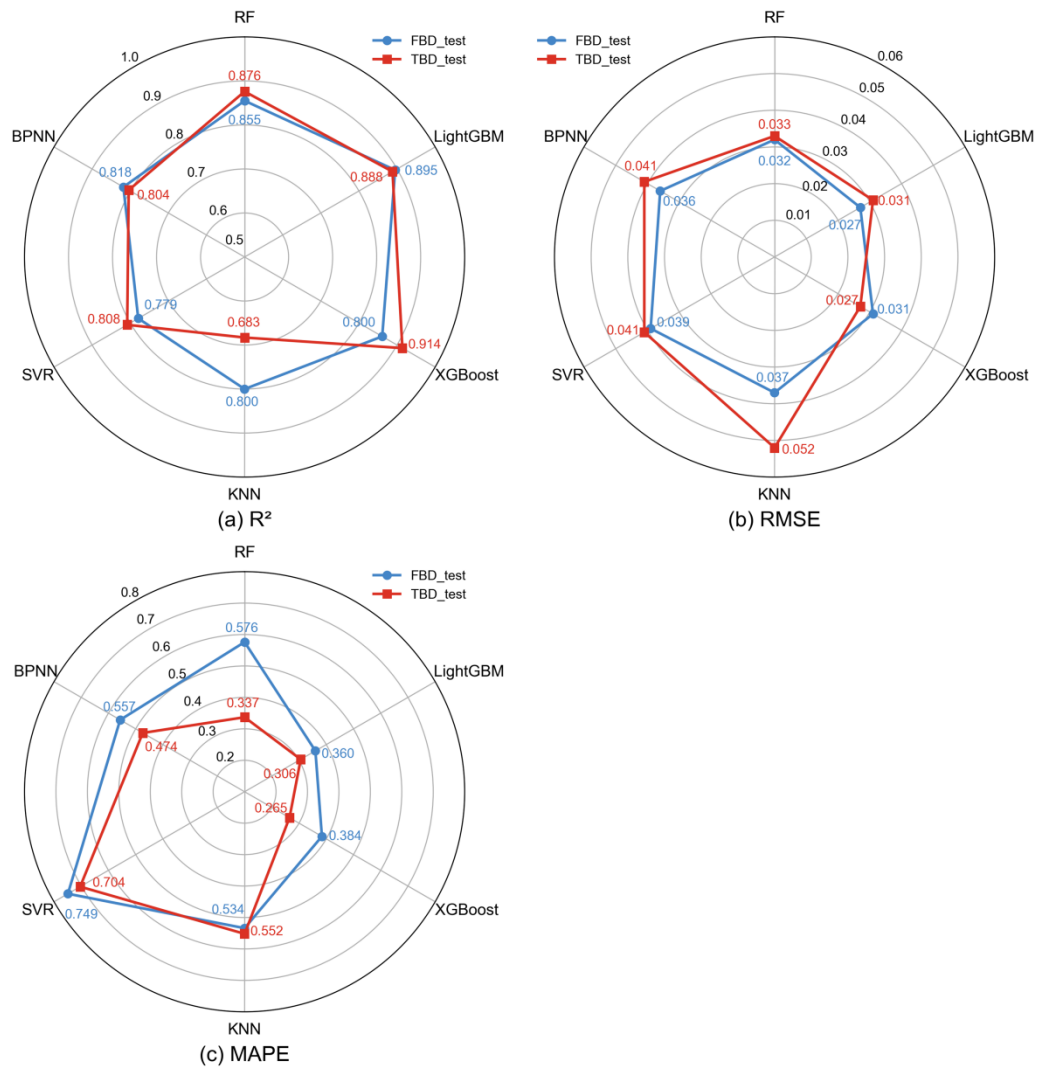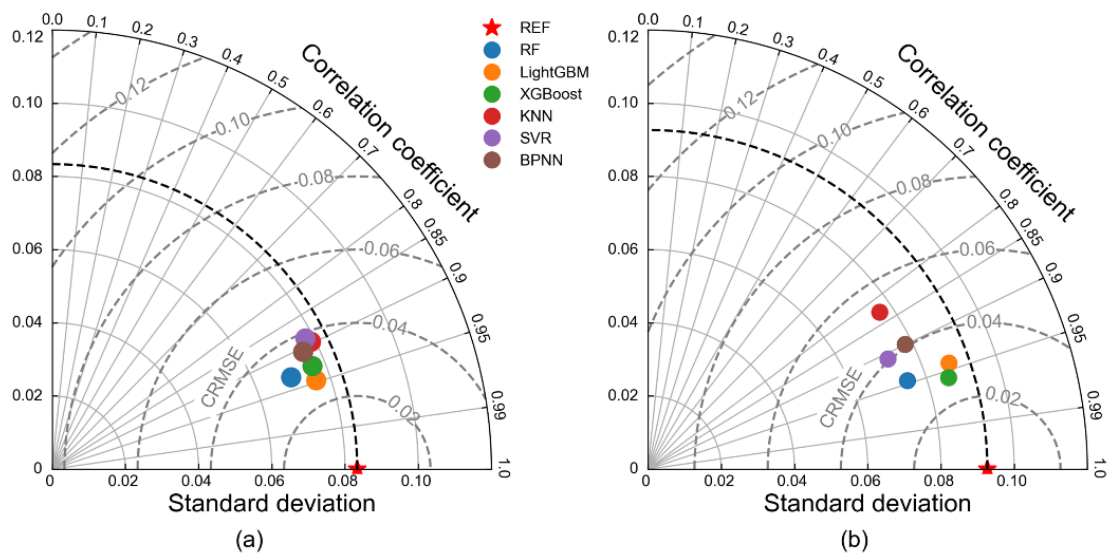917　　　　　　**Fig. 10 Performance of the six ML models on validation datasets**

918
919　　　　　　**Fig. 11 The R2 results for each fold on (a) FBD_val and (b) TBD_val**
920

921

922 **Fig. 12 Prediction results of the six ML models**

(a) R² (b) RMSE (c) MAPE

923
924 **Fig. 13 Performance comparison of the six ML models**
925

(a) (b)

926
927 **Fig. 14 Taylor diagrams of the six ML models on (a) FBD_test and (b) TBD_test**